JOURNAL OF GEOPHYSICAL RESEARCH, VOL. 106, NO. A12, PAGES 29,105–29,123, DECEMBER 1, 2001

First Tomographic estimate of volume distribution of HF-pump enhanced airglow emission

B. Gustavsson[1], T. Sergienko [1], M. T. Rietveld[3],
F. Honary [4],
Å. Steen[1], B. U. E. Brändström[1],
T. B. Leyser[2],
A. L. Aruliah [5],
T. Aso[6], M. Ejiri[6] and S. Marple[4]

Abstract. This report presents the first estimates of the three-dimensional volume emission rate of enhanced $O(^1D)$ 6300 Å airglow caused by HF radio wave pumping in the ionosphere. Images of the excitation show how the initially speckled spatial structure of excitation changes to a simpler shape with a smaller region that contains most of the excitation. A region of enhanced airglow was imaged by three stations in the Auroral Large Imaging System (ALIS) in northern Scandinavia. These images allowed for a tomography-like inversion of the volume emission of the airglow. The altitude of maximum emission was found to be around 235 ± 5 km with typical horizontal and vertical scale sizes of 20 km. The shape of the $O(^1D)$ excitation rate varied from flatish to elongated along the magnetic field. The altitude of maximum emission is found to be approximately 10 km below the altitude of the enhanced ion line and 15 km above the altitude of maximum electron temperature. Comparisons of the measured altitude and temporal variations of the 6300 Å emission with modelled emission caused by $O(^1D)$ excitation from the high energy tail of a Maxwellian electron distribution show significant deviations. The 6300 Å emission from excitation of the high energy tail is about a factor of 4 too large compared with what is observed.This shows that the source of $O(^1D)$ excitation is electrons from a "sub-thermal" distribution function, i.e. the electron distribution is Maxwellian at low energies and at energies above 1.96 eV there is a depletion.

1. Introduction

The phenomenon of high frequency (HF) induced intensification of airglow at 6300 Å and 5577 Å from the two lowest excited states of oxygen $O(^1D)$ and $O(^1S)$ has been studied since the early 1970s at low latitude (Arecibo) [*Sipler and Biondi*, 1972; *Carlson et al.*, 1982; *Bernhardt et al.*, 1989b], at mid latitudes (Platteville Colorado, Moscow, Sura) [*Haslett and Megill*, 1974; *Adeishvili et al.*, 1978; *Bernhardt et al.*, 1989b] and at auroral latitudes [*Stubbe et al.*, 1982; *Brändström et al.*, 1999].

Altitude estimates of the emission region have been achieved by triangulation based on data from scanning photometers by [*Haslett and Megill*, 1974] showing the approximate altitude of the maximum emission region to be between 250 km and 290 km altitude with typical horizontal scale sizes of 120 by 100 km, and by [*Adeishvili et al.*, 1978] showing that the emission region was 200 ± 40 km.

In this report the first estimates of the volume emission distribution are achieved through a tomographic inversion scheme. The resulting altitude and temporal distributions are compared with theoretical excitation models.

Theoretical modelling of the volume emission distribution has been done by *Bernhardt et al.* [1989b] for accelerated electrons as the excitation source of $O(^1D)$, and by *Mantas and Carlson* [1996] for excitation of

[1]Swedish Institute of Space Physics, Kiruna Division, Sweden

[2]Swedish Institute of Space Physics, Uppsala Division, Sweden

[3]Max-Planck Institut für Aeronomie, Germany, also at EISCAT, Ramfjordmoen, Norway

[4]Department of Communication systems, Lancaster University, UK

[5]Atmospheric Physics Lab., University College London, England

[6]National Institute of Polar Research, Tokyo, Japan

Paper number 2000JA900167.
0148-0227/01/2000JA900167$09.00

$O(^1D)$ from the tail of a purely thermal Maxwellian electron distribution. The two excitation mechanisms predict different altitude distributions of the volume emission as well as a different ratio between red(6300 Å)/green (5577 Å) intensities.

With detailed modelling of the aeronomy of the ionosphere-thermosphere system a temporal variation of the emission is obtained. Previously a model taking only the temperature variation of the direct electron impact excitation of $O(^1D)$ into account has been used [*Mantas*, 1994]. It has been shown that the temperature variation in the $O(^1D)$ source from dissociative recombination of O_2^+ has to be included, and that this gives a temporal evolution of the 6300 Å airglow which is inconsistent with what is observed [*Sergienko et al.*, 2000]. The calculated temporal variation is compared with the observed, and significant differences are found.

2. Experimental data

From 16:32 to 17:22 UT on 16th February 1999 the EISCAT Heating facility [*Rietveld et al.*, 1993] in Tromsø was operated at 4.04 MHz transmitting about 125 MW effective radiated power in ordinary mode with a 2-minutes-on and 2-minutes-off cycle to enhance airglow in the night time F-region ionosphere. From 17:24 to 18:32 UT the HF-pump cycle was changed to a 4 - minutes - on and 4 - minutes - off cycle.

During the experiment one, two, or three ALIS [*Steen and Brändström*, 1993] stations imaged the enhanced airglow simultaneously [*Brändström et al.*, 1999], the experimental setup is presented in Plate 1. For the period 17:40 to 17:56 UT the 6300 Å airglow was measured by the ALIS stations in Silkimuotka, Abisko and Nikkaluokta. Exposures were made synchronously every 10 s and the exposure time was 5 s.

For most part of the period from 16:32 to 18:32 UT modulations in the 6300 Å airglow were observed, that is both during the 2 minutes on 2 minutes off and the 4 minutes on 4 minutes off HF-pump modes. Even for the period with the lowest altitude of enhanced ion line the airglow modulation was observed as shown in Figure 1 where the maximum intensity in each image is plotted as a function of time. As can be seen there are some variations in the airglow imaged from Kiruna between 16:50 and 17:00 UT that correlate well with the heater cycle. Also some modification is seen in the maximum intensity of the Abisko images between 17:00 and 17:15 UT. However the clearest modifications were obtained between 17:30 and 18:30 UT when the enhanced ion line altitude was between 240 and 265 km and the EISCAT-Heating was operated in a 4 min on 4 min off cycle as previously reported by *Brändström et al.* [1999]. After 17:40 UT the Kiruna camera was directed to local zenith, imaging the natural background airglow. As can be seen there is a very good correlation between the signals from the different cameras and the modulation is well in phase with the HF-pump pulse. In the images the region of enhanced airglow is clearly seen (Plate 2) and the region of enhanced emission appears to move little during an individual pulse. The rise time of the emission is approximately a factor of two longer than the decay time.

During the entire experiment, background plasma parameter values such as the electron concentration, electron temperature and ion temperature (n_e, T_e, T_i) were measured using the EISCAT-UHF incoherent scatter radar, as shown in Plate 3. For this night time experiment we observed electron temperatures of up to 3500 K. This is in contrast to previously reported high latitude day time experiments [e.g. *Honary et al.*, 1993] that observed electron temperatures of approximately 2000 K. A discussion of the EISCAT UHF measurements has been presented by *Leyser et al.* [2000]; a more detailed analysis will be presented in a separate paper. In particular the variation during heating and cooling will be studied.

At the start of each HF-pump period, the incoherent scatter ion line spectrum measured by the EISCAT UHF (931 MHz) radar often showed a strong enhancement at the ion-acoustic peaks, often referred to as the enhanced ion-line overshoot. This ion line is usually (but not always) quenched in the second 5-s integration period. The ion line is caused by Langmuir turbulence just below the HF reflection height in which the HF-pump wave couples to electron plasma waves and ion acoustic waves [*Rietveld et al.*, 1993; *Stubbe et al.*, 1982]. This enhancement is also seen as a spike in the power profiles, one of which has 3.1 km range resolution. The height at which the enhancement occurs is known as the matching height because it is where the radar wavelength matches the wavelength of natural Langmuir waves which have the same frequency as

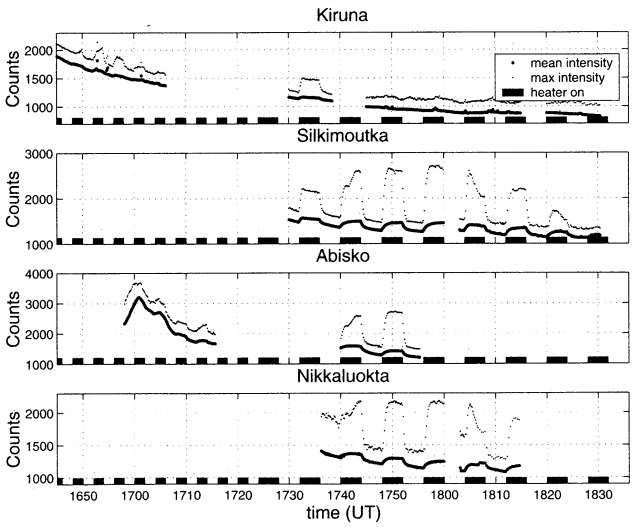

Figure 1. Maximum and average column emission of the 6300 Å airglow as seen from four stations. The intensity modulations correlate well with the heater on - off cycles. After 17:40 UT the Kiruna camera was directed to local zenith imaging the natural background airglow.

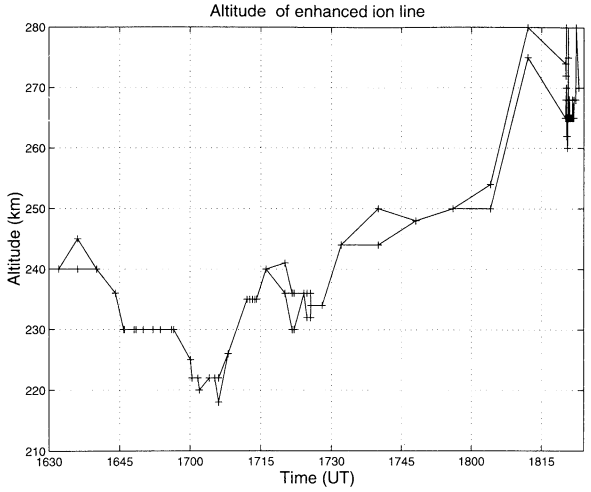

Figure 2. EISCAT UHF measurements of the altitude of the enhanced ion line. Comparing with Figure 1, the strongest airglow enhancements are obtained when the enhanced ion line altitude is between 240 and 255 km.

the HF-pump wave. For the UHF radar this may be as much as 10 km below the reflection height which is where the HF-pump frequency equals the cold plasma frequency. How much the matching height is below the reflection height depends on the electron temperature and the electron density gradient. For our experiment, using an electron temperature of 1100 K, the plasma frequency offset from that at reflection is 240 kHz. For a typical ionospheric plasma frequency gradient of 30 kHz/km this would be 8 km below reflection. Another important height is the upper-hybrid height, which is where the conversion of HF waves to electrostatic waves that heat the plasma is very efficient. At this height the thermal resonance instability is operative [*Gurevich and Milikh*, 1997] and here electron heating and the formation of striations arethought to occur in a narrow altitude region [*Stubbe*, 1996]. At the upper-hybrid height the plasma frequency offset from that at the reflection height depends only on the pump frequency and the gyro frequency and is 229 kHz in our case, or 7.6 km below reflection using the same gradient as above. Therefore the altitude of the enhanced ion line spike in the power profile gives us the upper hybrid height to within a km, and the reflection height which is about 8 km higher. For this experiment the enhanced ion line altitude varied from 220 km at 17:00 UT to 260 km at 18:20 UT; after that time the F-region electron density decreased so that no HF reflection occurred, as seen in Figure 2.

In addition the neutral wind velocity was measured from Kiruna by University College London Fabry-Perot interferometers (FPI) [*Aruliah et al.*, 1996] showing winds varying between eastward and north-eastward with velocities from 130 to 180 m/s, shown in Figure 3, with a wind of 150 ± 5 m/s at 42° ± 5° east at 17:45 UT.

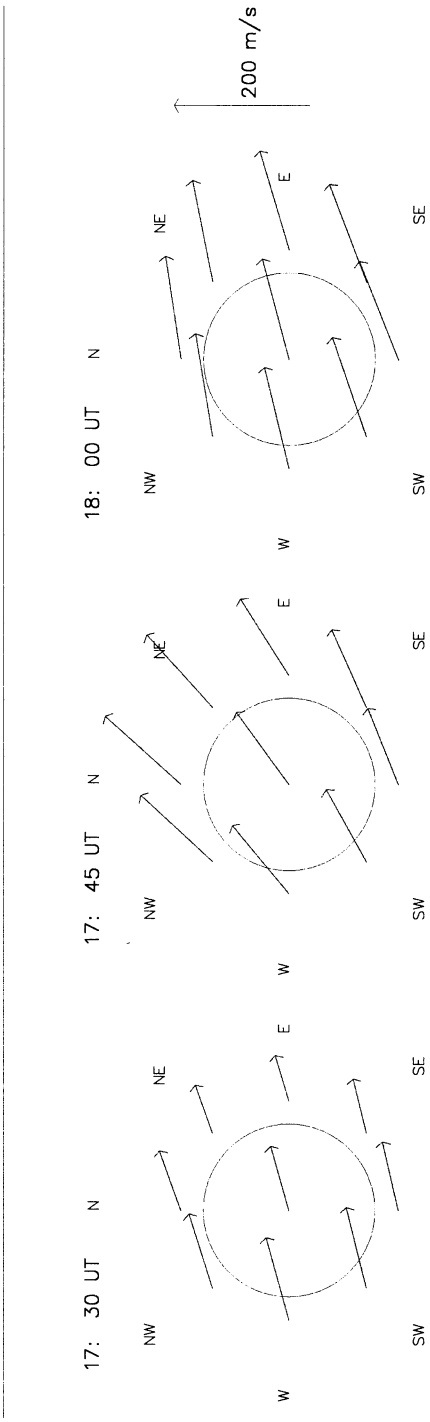

Figure 3. Fabry Perot interferometer (FPI) measurements of the neutral wind at 240 km altitude. The circle represents the field of view of the FPI looking at 45 degrees elevation. This represents a circle centered over Kiruna with a radius of approximately 240 km.

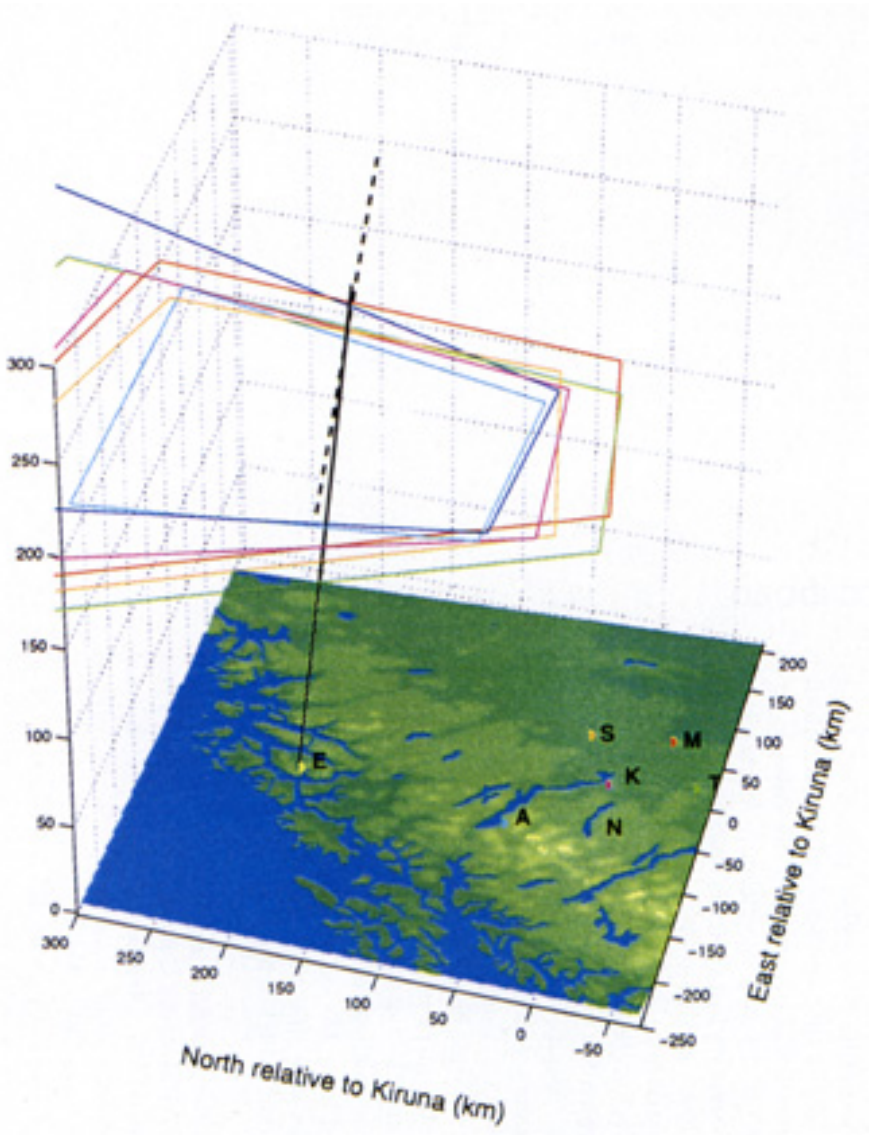

Plate 1. Geographic location of the EISCAT Heating facility and ALIS stations relative to Kiruna. The heater was directed 6° south and the local magnetic field at 250 km altitude has a declination of 13°.

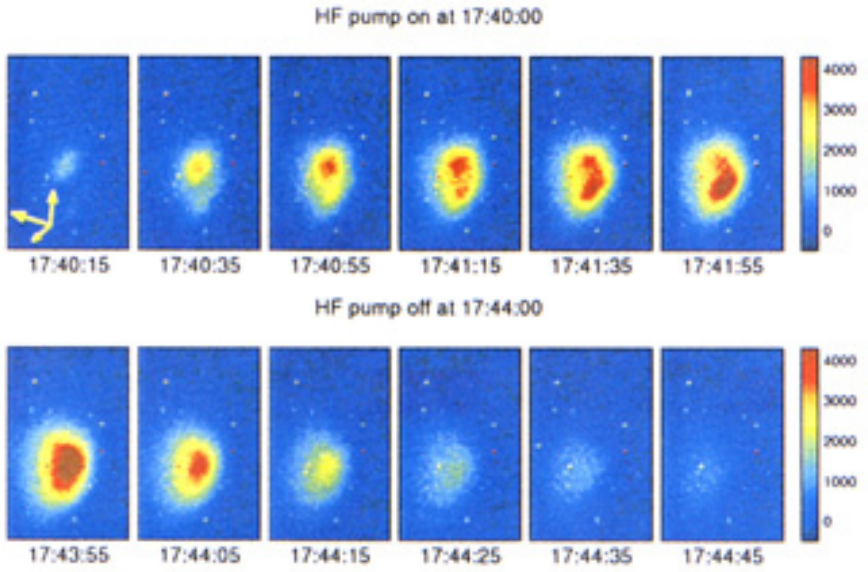

Plate 2. Typical time sequence for rise and decay evolution of the enhanced airglow region, as seen from Silkimuotka. Image intensity is shown in raw counts. The upper panels show the growth characteristics for a pulse where there are 2 separate regions of enhanced airglow. Here the initially fainter region out-grows the brighter region between 17:41:15 and 17:41:35 UT. The lower panels show the decay characteristics. Note that the time interval in the upper panels is 20 s and 10 s in the lower panels, thus showing that the decay is approximately a factor of 2 faster. The field of view is approximately 16° per side. The arrows in the top-left panel, starting with the near-vertical one and rotating clockwise, represents the north zenith and east directions.

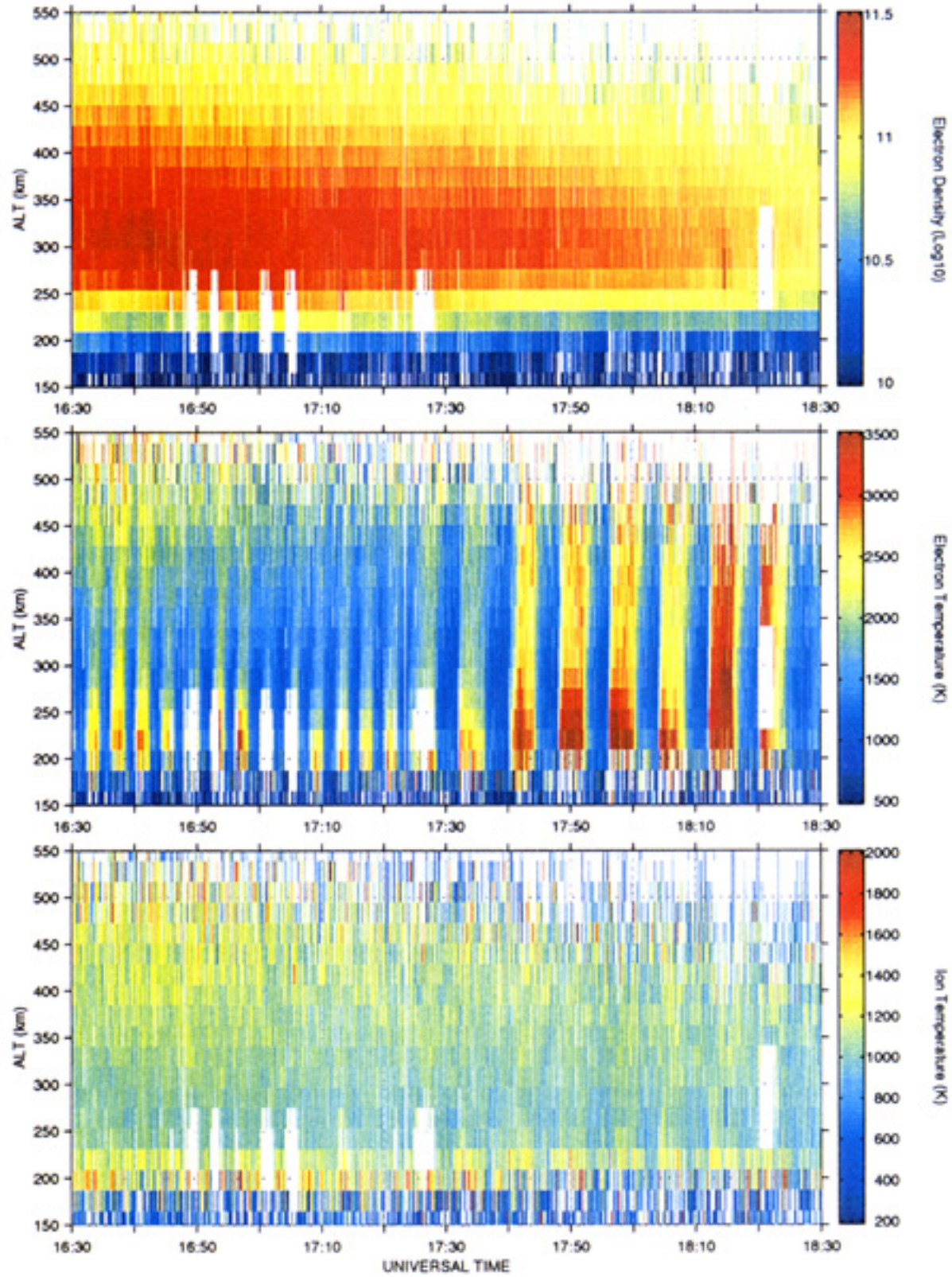

Plate 3. EISCAT UHF radar measurements of electron density (upper panel), electron temperature (middle panel) and ion temperature (lower panel) for 16 February 1999. The data are for altitude gates spaced 22.5 km apart, which were analysed with 5 s time resolution. The blank areas below 350 km altitude are regions where the ion line was enhanced by the HF-pump wave, causing the standard analysis to be invalid.

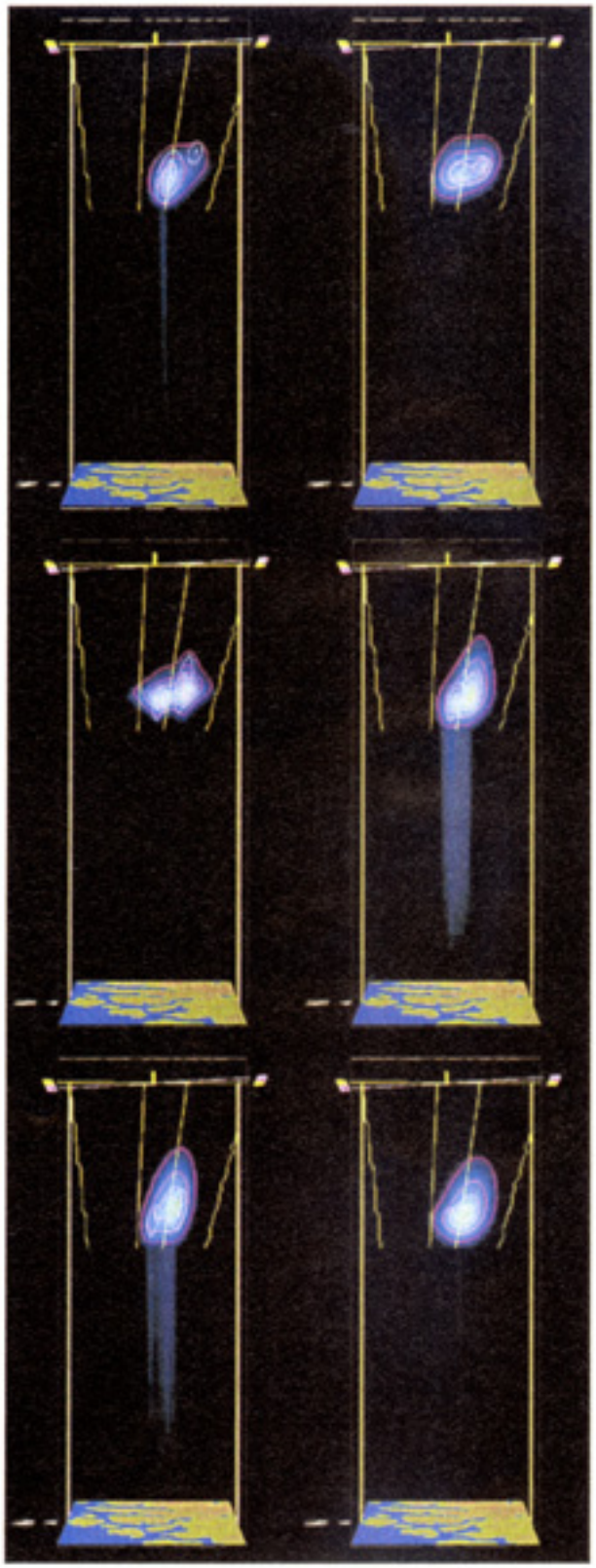

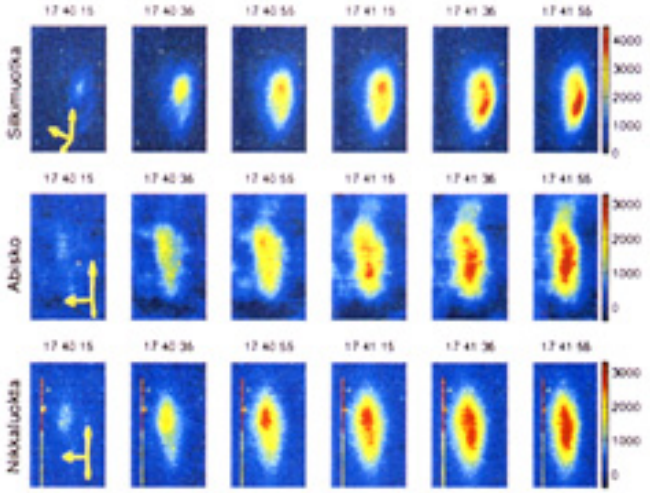

Plate 5. Volume rendering of the artificially enhanced airglow region above Tromsø, as seen from the west. The bottom plane shows the map of the Tromsø/Kiruna region. The yellow lines are the HF-Pump 70 % and 10 % beam widths in the meridional plane, the purple and orange contours are the 6300 Å emission and the $O(^1D)$ excitation. Upper left 17:32:50 UT, upper right 17:33:20 UT, middle 17:33:50 and 17:34:30 UT, bottom 17:34:50 and 17:35:20 UT.

Plate 4. The initial growth period of the pulse between 17:40 and 17:44 UT as seen from 3 stations, enhanced intensity is shown in counts. The light blue structures in the images from Abisko are due to clouds in the lower atmosphere. The arrows are clockwise from vertical the projection of: north, zenith and east directions.

3. Solution of the inverse problem

The problem of determining the volume emission intensities of the enhanced airglow from multi-station imaging is a tomographical problem where, starting from a set of image projections of the airglow, its inner spatial distribution is to be determined. In most cases these tomographic problems are ill-posed, but with some regularization schemes (i.e. physical or mathematical constraints) the problem can in a restricted sense be transformed to a well-posed problem [*Ghosh Roy*, 1991]. Auroral and airglow tomography from ground-based multi-station measurements is ill-posed due to the facts that only a few projections/images of the aurora are available and that the image observations are all made from below the object and thus are close to being linearly dependent.

Several regularization schemes have recently been used [*Aso et al.*, 1998; *Semeter*, 1997] and proposed [*Gustavsson*, 1998] to solve the ground-based tomographic inverse problem. For the particularly ill-posed problem discussed here, with measurements from only three stations south of the emission region and spanning only a limited angular range, we have to use an even more constrained method to determine the volume emission rate. Our choice is to use a model function that can describe the spatial variation of the airglow emission with only a few free parameters and to search for a set of parameters that produce an airglow distribution which gives image projections similar to the original images. This search is done by minimisation of the total least square error function

$$f(\bar{V}_i) = \sum_{s,u,v} \left[p_s(u,v) - \tilde{p}_s(u,v,I(\bar{r},\bar{V}_i)) \right]^2 \qquad (1)$$

where $p_s(u,v)$ is the image intensity within pixel (u,v) after background reduction, in the image taken at station s and $\tilde{p}_s(u,v,I(\bar{r},\bar{V}_i)$ is the corresponding image intensity calculated from the model airglow $I(\bar{r},\bar{V}_i)$ through the forward model

$$\tilde{p}_s = \boldsymbol{F}_s(I) \qquad (2)$$

describing the imaging process. Finally V_i is the parameter set searched for.

3.1. The imaging process - forward model

To calculate the image projections that an airglow model function would cause, $I(\bar{r},t)$ is calculated on a three-dimensional grid with 32 volume elements in each direction. The south-west lower corner of this block is located 113 km west, 112 km north of Kiruna at an altitude of 205 km and the side length of an individual volume element (voxel) is 4 km. This discrete representation of the airglow emission is then projected down to the image planes of the ALIS stations.

For the projection of the model airglow to the image planes the greatest care necessary has been taken to determine the pixel lines of sight, known to within $\pm 0.01°$, and the pixel fields of view, known to within $\pm 0.01\%$. The line of sight uncertainty corresponds to approximately 20 % of the field of view of a pixel; thereby we can get the highest positioning accuracy possible with ALIS.

Unfortunately the ALIS project still lacks reliable and accurate intensity calibration for pixel sensitivity. However, for the cameras in Silkimuotka, Abisko and Nikkaluokta average relative sensitivity factors exist. The forward model or the projection operation takes the following factors into account: intersection between the pixel field of view and the voxel, the atmospheric absorption, and the effective area of the front lens, $A_{lens} \cdot \cos\theta$, where θ is the angle between the pixel line of sight and the optical axis.

3.2. Model airglow

An airglow model function should take the basic physical processes of diffusion, drift, and the altitude variation of $O(^1D)$ effective lifetime into account. To construct such a model function we look at the continuity equation for the $O(^1D)$ number density n

$$\frac{\partial n}{\partial t} + \bar{v} \cdot \nabla n + n \nabla \cdot \bar{v} + D \nabla^2 n = Q(\bar{r},t) - L(z) \qquad (3)$$

where $\bar{v}$ is the neutral wind, D is the $O(^1D)$ diffusion coefficient, L is the total loss rate of $O(^1D)$, and Q is the space and time dependent $O(^1D)$ excitation rate.

Since the region with enhanced airglow is small compared to the typical scale size for variations in the neutral wind field $\bar{v}$, the wind is assumed to be constant over the entire region and thus it is possible to neglect the divergence term $n_{(O^1D)} \nabla \cdot \bar{v}$. In equation (3) we have neglected the altitude variation of the diffusion and the thermal diffusion factors. For a more complete three-dimensional forward modelling of gas diffusion see *Bernhardt* [1979]. The reason for this simplification as well as the other mentioned below is that we will use this continuity equation to derive a suitable model function to use in solving the three-dimensional emission tomography problem. Thus we need a model that takes the basic physical processes into account, but since the optimisation of equation (1) requires $1 \cdot 10^4 - 1 \cdot 10^8$ evaluations of the model function over a three-dimensional grid it is preferable if the model function allows for numerical evaluation such that the optimisation can converge within hours on the computers available today.

Q in equation (3) is the space dependent excitation rate of $O(^1D)$ at point $\bar{r}$ and time t_i, for which any function can be used. The demands on the excitation function are that it should have a maximum and decrease away from that maximum, it should be specified by a few parameters and yet have some flexibility to change shape. A compromise that fulfills our needs is a generalised Gaussian

$$Q(\bar{r},t_i) = Q_i \cdot \exp\{-[\{\frac{x'^{\alpha_i}}{\sigma_{xi}^{\alpha_i}} + \frac{y'^{\alpha_i}}{\sigma_{yi}^{\alpha_i}}\}^{2/\alpha_i} + \frac{(z-z_i)^2}{\sigma_{zi}^2}]^{\gamma_i}\} \quad (4)$$

where Q_i is the maximum excitation rate and

$$x' = (x - x_i)\cos\beta_i + (y - y_i)\sin\beta_i \quad (5)$$

and

$$y' = (y - y_i - (z - z_i)\cdot\sin\phi_m)\cos\beta_i - (x - x_i)\sin\beta_i \quad (6)$$

Here (x_i, y_i, z_i) is the point of maximum $O(^1D)$ excitation; x is positive eastward, y is northward, z is in Kiruna local zenith and ϕ_m is the local magnetic inclination, $(\sigma_{xi}, \sigma_{yi}, \sigma_{zi}^-, \sigma_{zi}^+)$ are the corresponding widths where σ_{zi}^- is used below z_i and σ_{zi}^+ is used above z_i. β_i is the rotation angle of the excitation ellipsoid around the vertical, and γ_i and α_i are shape parameters.

Since the 6300 Å airglow is proportional to the $O(^1D)$ concentration, direct integration of equation (3) gives us a model function $I(\bar{r},t)$ for the enhanced 6300 Å airglow. Due to the long effective lifetime of $O(^1D)$ in the F-region ionosphere in the altitude range 200–300 km we cannot neglect the effects of drift and diffusion when integrating equation (3)

$$I(\bar{r},t) = \sum_{j=1}^{i} \exp(-(t_i - t_j)/\tau_z) \cdot Q(\bar{r_j} - \int_{t_j}^{t_i} \bar{v}(t')dt', t_j) \otimes \left(\frac{\pi^{-3/2}}{[\int_{t_j}^{t_i} D(t')dt']^{1.5}} \exp(\frac{-|\bar{r}|^2}{\int_{t_j}^{t_i} D(t')dt'})\right) \quad (7)$$

where τ_z is the effective lifetime of $O(^1D)$ and $\otimes$ denotes three-dimensional convolution over $\bar{r}$. This model function has the following set of free parameters to be determined for the images from time t_i

$$\bar{V}_i = < Q_i, x_i, y_i, z_i, \sigma_{xi}, \sigma_{yi}, \sigma_{zi}, \gamma_i, \alpha_i, \beta_i, D_i, \bar{v}_i > \quad (8)$$

Here it should be noted that the airglow emission distribution at time t_i not only depends on the simultaneous $O(^1D)$ excitation but also on the preceding excitation. For example the drift term, $\int_{t_j}^{t_i} \bar{v}(t')dt'$ accounts for the drift from t_j to t_i of $O(^1D)$ excited at t_j, while x_i, y_i, z_i, the center of the excitation function Q at t_i, is an independent free parameter accounting for the motion of the excitation. This latter motion has been attributed to the $\bar{E} \times \bar{B}$ drift [*Bernhardt et al.*, 1989a]. The loss processes for $O(^1D)$ that are taken into account when calculating τ_z are quenching, that is collisional de-excitation, by collisions with molecular oxygen and nitrogen,

$$O(^1D) + N_2 \xrightarrow{q_1} O(^3P) + N_2 \quad (9)$$

$$O(^1D) + O_2 \xrightarrow{q_2} O(^3P) + O_2 \quad (10)$$

with the rate coefficients [*Mantas and Carlson*, 1996]

$$q_1 = 2.0 \cdot 10^{-11} \exp(107.8/T_n) \text{ cm}^3\text{s}^{-1} \quad (11)$$

$$q_2 = 2.9 \cdot 10^{-11} \exp(67.5/T_n) \text{ cm}^3\text{s}^{-1} \quad (12)$$

and with atomic oxygen

$$O(^1D) + O \xrightarrow{q_3} O(^3P) + O \quad (13)$$

with the rate coefficient [*Solomon et al.*, 1988]

$$q_3 = 2.0 \cdot 10^{-12} \text{ cm}^3\text{s}^{-1} \quad (14)$$

The importance of quenching by atomic oxygen has been under some debate [*Link and Cogger*, 1998; *Solomon et al.*, 1988]. Further $O(^1D)$ is quenched by thermal electrons,

$$O(^1D) + e \xrightarrow{q_4} O(^3P) + e \quad (15)$$

with a quenching rate [*Rees*, 1989]

$$q_4 = 1.6 \cdot 10^{-12} T_e^{0.91} \text{ cm}^3\text{s}^{-1} \quad (16)$$

and by radiative transfer [*Fischer and Saha*, 1983]

$$O(^1D) \Rightarrow \begin{cases} O(^3P_2) + h\nu(\lambda = 6300\text{Å}) & (17) \\ O(^3P_1) + h\nu(\lambda = 6364\text{Å}); & (18) \\ O(^3P_0) + h\nu(\lambda = 6392\text{Å}) & (19) \end{cases}$$

with the respective transition probabilities $A_2 = 0.0071\ s^{-1}$, $A_1 = 0.0022\ s^{-1}$ and $A_0 = 1.1 \cdot 10^{-6}\ s^{-1}$, giving a total radiative de-excitation probability of the $O(^1D)$ state: $A_{O(^1D)} = A_0 + A_1 + A_2$ corresponding to an effective radiative lifetime of 107 s. For the neutral densities we use the MSIS-90 atmospheric model [*Hedin*, 1991], and the EISCAT UHF measurements contribute with measurements of n_e and T_e. The collision rate coefficients depend on the neutral temperature T_n for which we take $T_n \approx T_i$ where the EISCAT UHF ion temperature T_i is used. The ion temperature should be fairly close to the neutral temperature when there are no large electric fields, as was the case during the quiet magnetic conditions of this experiment.

3.3. Determination of model parameters

Now we can rewrite equation (1), the total error function, to

$$f(\bar{V}_i) = \sum_{s,u,v} [p_s(u,v) - \tilde{p}_s(u,v,I_i(\bar{V}_i, I_{i-1}))]^2 \quad (20)$$

Here it should be noted that the volume emission distribution $I_i(\bar{V}_i, I_{i-1})$ given by equation (7) not only depends on the excitation Q at time t_i but, due to the long lifetime of $O(^1D)$, also on the excitation at $t < t_i$. This dependency can be reformulated in such a way that the emission at t_i depends on the immediate excitation and on the emission at t_{i-1}. To determine the $O(^1D)$ excitation and airglow emission at time t_i we also need to know the excitation and emission at times $t < t_i$, thus we estimate the free parameters $\bar{V}_i$ for one set of images at a time starting at 17:40:05 UT and then stepwise for the consecutive sets of images giving a time series of the parameter set.

To determine the free parameters in $\bar{V}_i$, we minimise $f(\bar{V}_i)$ in equation (20) using the "optimised step size random search optimisation method" [*Belur*, 1979] where the parameters $(Q_i, \sigma_{xi}, \sigma_{yi}, \sigma_{zi}, D)$ are constrained to be positive. The maximum excitation point is constrained to lie within a box $(-100 < x_0 < 0, 120 < y_0 < 220, 180 < z_0 < 280,)$, and the final constraint is $\gamma > 0.1$. For the neutral wind we use the FPI measurements as initial estimates. To get a fit with the image data in Plate 4 showing two peaks it is necessary to extend the model to contain two $O(^1D)$ excitation sources as described by equation (4). However only one set of values is used for the neutral wind $\bar{v}$ and diffusion parameter D.

With this approach of a simplified solution of a continuity equation for $O(^1D)$ the resulting parameters not only give us an estimate of $I(\bar{r}, t)$, the three-dimensional emission, but also a direct estimate of $Q(\bar{r}, t)$, the excitation rate of $O(^1D)$, as well as an estimate of the neutral wind.

A drawback with the discretisation is that there might be aliasing effects that make direct interpretations of the parameters difficult, a problem that is also made difficult by the fact that the parameters for the excitation widths, $\sigma_x, \sigma_y, \sigma_z$, the shape parameters, α, β, γ and the diffusion parameter D are far from independent. This is a consequence of the fact that a true airglow emission distribution with unknown shape in an atmosphere with a diffusion coefficient D is best modelled with shape parameters γ', α', D' where $D \neq D'$.

4. Data and Analysis

For several HF-pump pulses two or three ALIS stations imaged the enhanced airglow. For the two HF-pump wave on off periods from 17:40 to 17:44 UT and 17:48 to 17:52 UT, for which observations from three ALIS stations are available, the tomography-like inversion analysis outlined in section 3 gives reliable results. For the other HF-pump periods for which data from two ALIS stations are available the inversion gives results that are less accurate. For these periods we can, however, obtain stereoscopic triangulations of the position of the enhanced airglow region.

4.1. Estimate of volume emission rate

For the two HF-pump wave on–off periods from 17:40 to 17:56 UT for which observations from three ALIS stations are available the tomography-like inversion analysis outlined in section 3 has been applied. i. e. for these two pulses we have obtained an estimate of the three-dimensional distribution of emission of the 6300 Å airglow and its time variation.

In the volume distribution of the airglow emission and the vertical contour cut through the centers of emission it can be seen that the existence of two separable regions is indisputable and that the shape of the excitation varies from prolate aligned along the magnetic field to slightly oblate, as shown in the volume renderings in Plate 5. The variation in shape is large but for the HF-pulse 17:40–17:44 UT the initially stronger region is by and large spherical while the second southward region is prolate aligned along the magnetic field. For the initial part of the HF-pulse 17:40 17:44 UT the weaker region starts as a narrow region in both altitude and latitude. After it starts to intensify it rapidly grows in size, mainly in the direction of the magnetic field.

To validate the accuracy of the retrieved enhanced airglow distribution we have to compare the measured image data with the image projections of the retrieved airglow. For the whole period the projections of the emission distribution and the observed images agree well with typical maximum errors of ±10%. The observed images and the resulting image projections of the estimated airglow distribution for 17:40:55 UT can be studied in Plate 6. As can be seen, the residuals show no (Silkimuotka, Nikkaluokta) or little (Abisko - clouds) structure, indicating good convergence of the parameter set. As can be seen in the fourth panels of Plate 6, one factor causing large errors is minor deviations in the widths of the airglow regions, leading to large errors where there are sharp gradients in intensity. Another likely cause of large errors is that even for the optimal set of parameters the model functions cannot give an airglow distribution that exactly agrees with the true one. The reason for this might be that the $O(^1D)$ excitation distribution did not have a shape that was a generalised Gaussian, or that the airglow region consisted of more than two excitation regions.

To obtain two regions of volume emission and a fit between the projected and the observed images with more than one maxima in enhanced airglow, two source functions Q_1 and Q_2 according to equation (4) are necessary. This gives us two sets of the parameters $< Q_i, x_i, y_i, z_i, \sigma_{xi}, \sigma_{yi}, \sigma_{zi}, \gamma_i, \alpha_i, \beta_i, >$. However only one set of values is used for the diffusion parameter D and neutral wind $\bar{v}$.

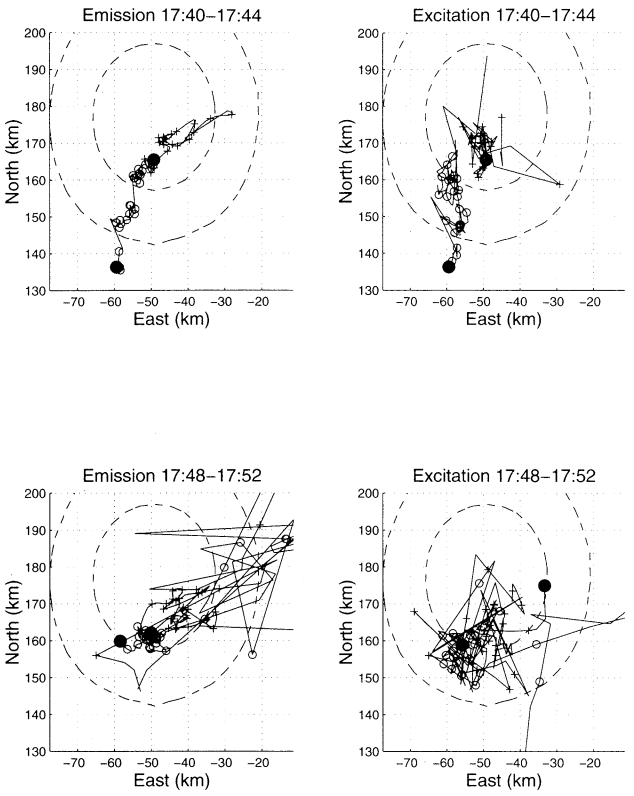

Figure 4. Upper left: trajectories of the centers of 6300 Å airglow emission, starting at the black points. Upper right, centers of $O(^1D)$ excitation. Lower left, centers of 6300 Å airglow emission. Lower right, centers of $O(^1D)$ excitation. It is 10 seconds between the markers in all panels and all distances are relative to Kiruna. The dashed contours are the -1 and -3 dB projections of the HF-pump beam.

To separate the enhanced airglow from the natural variations in the $O(^1D)$ nightglow, the images taken at 17:39:55, 17:47:55 and 17:55:55 UT just before the HF-pump at 17:40:00,17:48:00 and 17:56:00 UT were used as "background" images and linear interpolation pixel by pixel was used to remove the background.

In addition to the uncertainties in the relative sensitivities of the ALIS cameras the thin drifting cloud cover in Abisko creates a further problem regarding the intensity in those images relative to the other stations. To overcome this problem the images and model projections from Abisko are normalised by their respective maximum intensities. By doing this the data from Abisko contribute information on the shape of the enhanced airglow but not on the absolute intensity.

4.2. Analysis of volume emission distribution

In this first analysis of the volume emission distribution we will use the same methods used by *Bernhardt et al.* [2000] and concentrate on the altitude distribution, the drift pattern, the total 6300 Å emission rate,

$$I_{tot}(t_i) = \int I(\bar{r}_i, t_i) dV \tag{21}$$

and the total $O(^1D)$ excitation rate

$$Q_{tot}(t_i) = \int Q(\bar{r}_i, t_i) dV \tag{22}$$

where $I(\bar{r}_i, t_i)$ is calculated as in equation (7) and $Q(\bar{r}_i, t_i)$ is calculated as in equation (4). Since the parameter set V_i is determined by minimisation of equation (20), where the airglow emission is calculated on a discrete set of voxels, we have to calculate the total airglow emission and $O(^1D)$ excitation via the discretised voxel space to avoid possible aliasing problems. In the same manner rather than taking the values of $\bar{r}_i$ from the optimal parameters we prefer to calculate the center of emission

$$\bar{r}_{ce}(t_i) = \int \bar{r} I(\bar{r}, t_i) dV / \int I(\bar{r}, t_i) dV \tag{23}$$

and the center of excitation

$$\bar{r}_{cx}(t_i) = \int \bar{r} Q(\bar{r}, t_i) dV / \int Q(\bar{r}, t_i) dV \tag{24}$$

Calculation of the "centers of emission and excitation" shows that there are significant differences between the two pulses. As is seen in Figure 4, during the 17:40 UT pulse cycle the initial location of the two interaction regions are approximately 20 to 30 km apart and the northernmost region of excitation (the initially more intensive) is fairly immobile while the southernmost moves 30 km northward in 4 minutes corresponding to a velocity of $100 \pm 20 m/s$. The north-eastward drift of the "center of emission" agrees well with the FPI measurements of the neutral winds.

Looking at the total $O(^1D)$ excitation Q_{tot} and airglow emission I_{tot} for the two studied pulses it is found that for the first pulse cycle from 17:40 to 17:44 UT, when there existed two distinct excitation regions, the excitation rate of the initially stronger region reached its maximum approximately one minute after HF-pump wave-on and then decayed, as can be seen in Figure 5. The total excitation rate in the initially weaker region grows continuously to the end of the HF-pump pulse. Comparing the "centers of emission" and "centers of excitation" and the projection of the antenna pattern of the HF-pump beam, it seems that the initially stronger region of excitation appeared closer to the center of the HF-pump beam while the second region of excitation appeared at the upwind -3 dB edge and grew in intensity as it drifted towards the center of the HF-pump beam.

These drift patterns and intensity variations can be understood as consequences of the fact that the energy dissipation of the HF-pump wave depends on the background ionosphere. Assuming that the HF-pump wave is preferentially dissipated in local density depletions, the strongest portion of the HF-pump beam could then create its own density depletion and pre-existing depletions drifting into the HF-pump beam can dissipate an

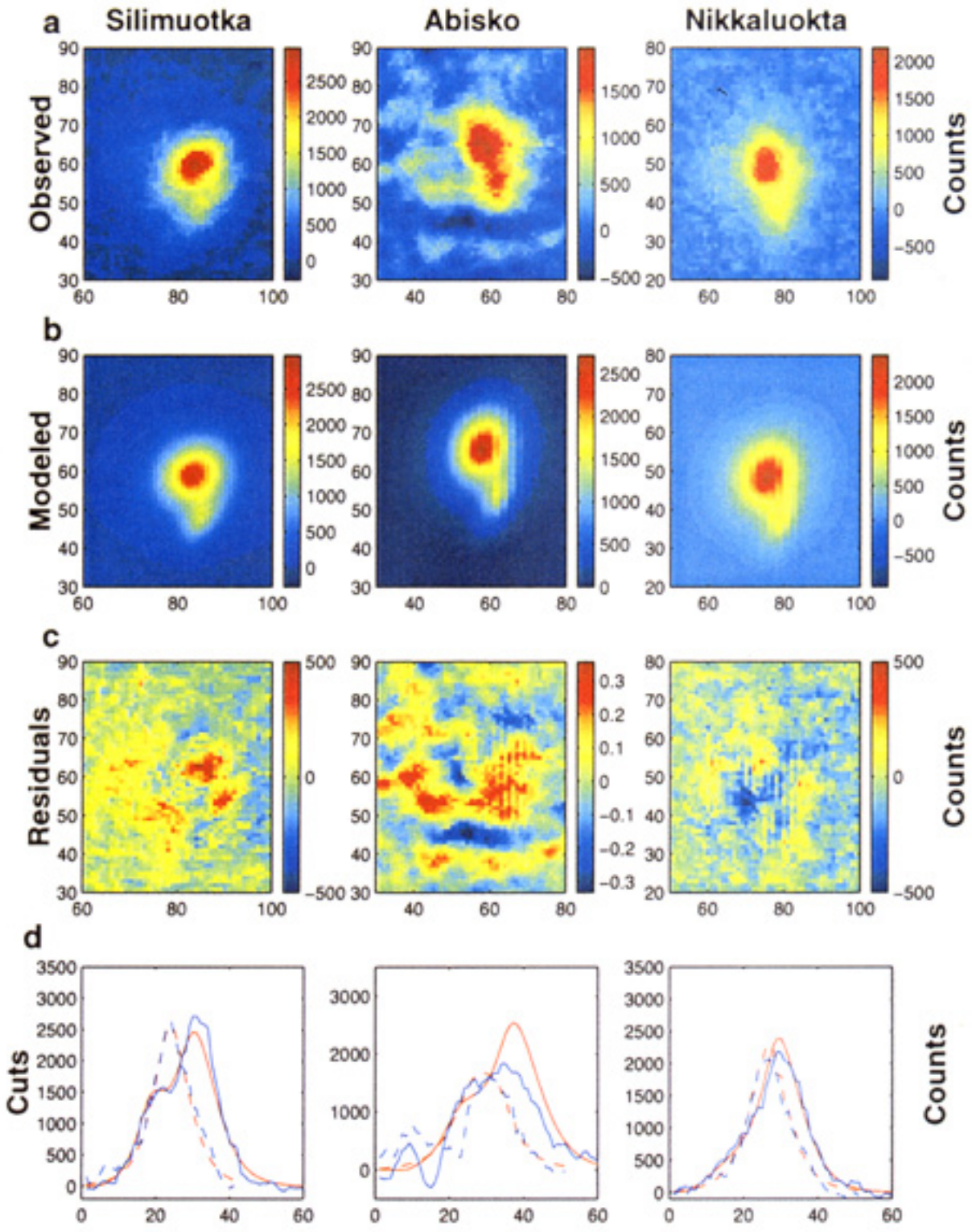

Plate 6. Upper panels: Observed artificial airglow at 17:40:45 UT, from left as seen from Silkimuotka, Abisko (slightly cloudy) and Nikkaluokta. Second panels: Projections of the reconstructed airglow. Third panels: Differences. For Abisko the image and the projection from the reconstruction are rescaled from 0 to 1 due to the faint clouds. Bottom panels: solid curves represent vertical columns, dashed curves horizontal rows, blue original data and red projections from the reconstruction. For Silkimuotka the horizontal row is number 57, and the vertical column is number 85. For Abisko the horizontal row is number 60 and the vertical column is number 60. For Nikkaluokta the row is number 50 and the vertical column is number 75.

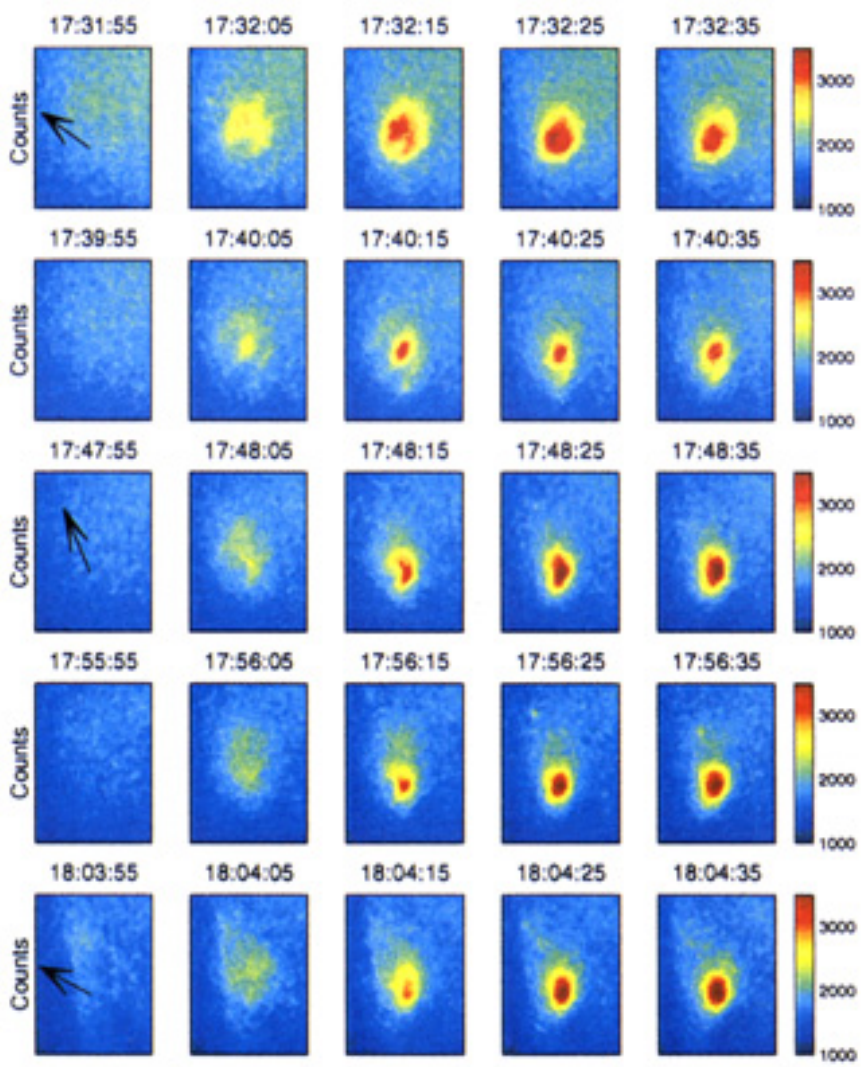

Plate 7. Estimates of the $O(^1D)$ excitation rates, $Q = I(t_i) - I(t_{i-1} \exp(-(t_i - t_{i-1})/34)$, for the period just before pulse on and the four 10 s periods just after pulse on for five pulses. The arrows are the neutral wind direction projected to the images from Silkimuotka.

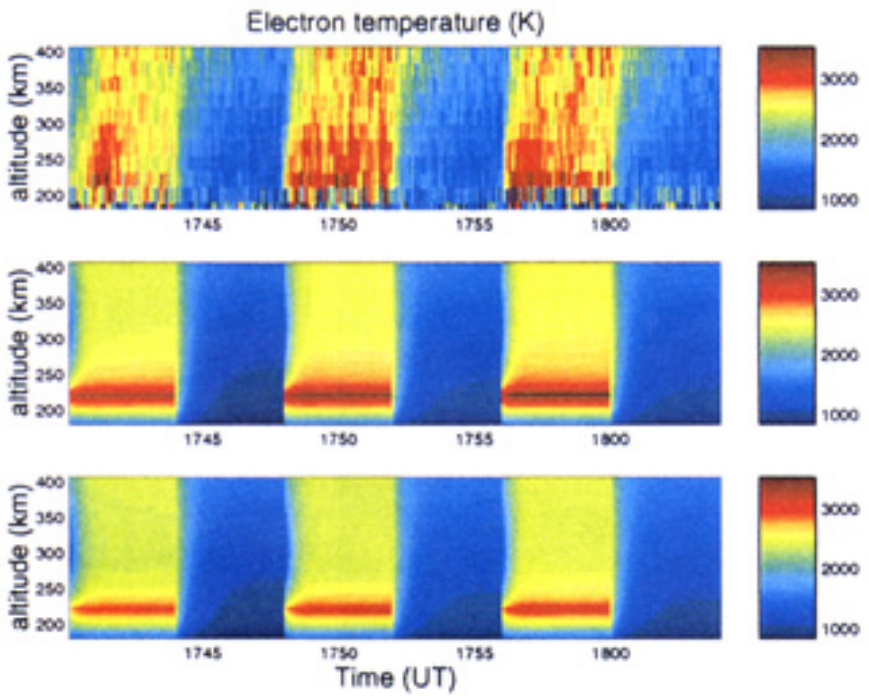

Plate 8. Upper panel: EISCAT UFH measurements of electron temperature. Middle panel: Modelled electron temperature with best fit of temperature. Bottom panel: Modelled electron temperature giving best fit with optical data.

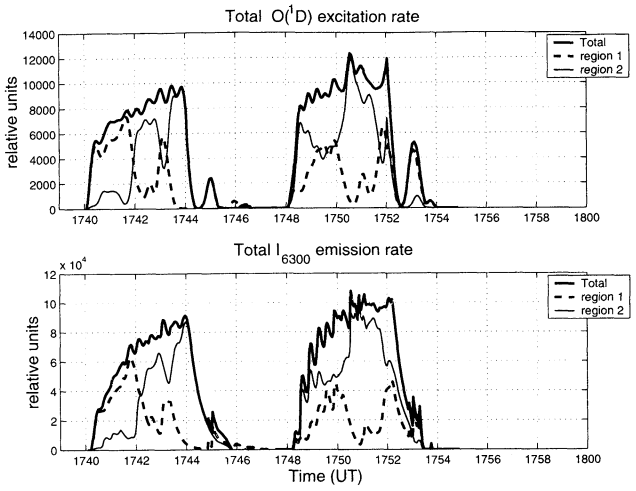

Figure 5. Upper panel, total $O(^1D)$ excitation rate for the two regions. Lower panel, total $O(^1D)$ emission rate for the two regions. "Region 1" corresponds to the trajectory marked with "+" in Figure 4 and "Region 2" to the trajectory marked with "o".

amount of energy that gives enough $O(^1D)$ excitation to appear as separate regions of enhanced airglow.

For the second pulse cycle between 17:48 and 17:52 UT more than one region of emission is possibly observed only during the first 15 s. Thus only the total emission and excitation describe a physical evolution. There the temporal evolution is fairly simple and shows that the excitation is approximately proportional to $1 - \exp(-t/20)$.

The existence of two regions with different growth characteristics in the emission, which are distinguishable for an extended period of time for the HF-pulse starting at 17:40 UT, can be seen in the images from the three stations presented in Plate 4. There it can also be seen that the initially fainter region is outgrowing the initially brighter region between 17:41:15 and 17:41:35 UT.

According to *Bernhardt et al.* [1989b] the altitude-averaged effective lifetime τ_a is

$$\tau_a^{-1} = \frac{\int I(z)/\tau(z)dz}{\int I(z)dz} \tag{25}$$

By applying this equation through the points of maximum emission for the two HF-pump pulses we obtain an altitude-averaged effective lifetime of 25 ± 2 s during the pulses and 30 ± 2 s for the first minute after the pumping. This altitude-averaged effective lifetime agrees to within 2 s with the effective $O(^1D)$ lifetime at the altitude of maximum emission.

4.3. Initial enhancement

By applying the above altitude-averaged effective lifetimes and neglecting transport processes it is possible to make a model-independent estimate of the altitude-averaged excitation distribution *Bernhardt et al.* [1989b]

$$\tilde{Q}(t_i) \propto D(t_i) - D(t_{i-1}) \cdot \exp(-[t_i - t_{i-1}]/\tau_a) \tag{26}$$

where τ_a is 30 s, $D(t_i)$ is the image exposed at t_i and $D(t_{i-1})$ is the image exposed at t_{i-1}. When calculating $\tilde{Q}(t_i)$ for the time just after the HF-pump on, a systematic pattern appears: the initial excitation shows a patchy structure but after some 15 - 25 seconds the excitation grows in a smaller region and the excitation in the surrounding region either saturates or even decreases, as is shown in Plate 7. The typical size of these initial speckles is approximately 5–15 km across. This initially complex structure of the excitation region has not been previously reported but the deepening-narrowing might be optical evidence of the self focusing that has been suggested by several authors, e.g. *Duncan and Behnke* [1978] and *Farley et al.* [1983]. For the pulses at 17:32 and 17:40 UT it appears as if the enhanced patches that are upwind of the most intensive region continue to intensify while the enhanced patches downwind of the most intensive region appear to convect out of the pump-ionosphere interaction region.

This initial patchiness of the excitation and the existence of two separate enhanced regions for more than 2 minutes indicate the importance of the initial background ionospheric conditions for the enhancement of artificial airglow. The decay of the downwind region and the growth and drift into the main region of the upwind regions indicate the importance of initial ionospheric conditions. Together with the result of the volume emission above, this indicates that the enhanced artificial airglow at high latitudes, rather than being a stable process, is a process controlled by the dynamics of the ionosphere.

4.4. Altitude estimation by triangulation

For the HF-pump pulses for which observations were made from at least two stations, triangulation of the point of maximum emission is made. Previously [*Brändström et al.*, 1999] this was done automatically by calculating the mid point of the shortest intersection between the lines of sight of the brightest points in the images from the available ALIS stations. With manual identification of the corresponding points it is now possible to estimate the altitude of the airglow for two additional pulses. Only points for which the shortest intersection is less than 5 km are considered reliable.

The result of the triangulation shows that the estimate of maximum emission altitude varies between 230 and 240 km from 17:32 to 18:08 UT, but for the HF-pump wave pulse starting at 18:12 UT the enhanced airglow altitude is between 250 and 260 km, as can be seen in Figure 6. The geometrical accuracy of the triangulation obtained by ALIS for a point source is less than $\pm$ 0.5 km, but taking measurement noise and the size of the emitting region into account a reasonable estimate of the accuracy in altitude is ± 3 km. Thus it is seen that the altitude of maximum emission is sys-

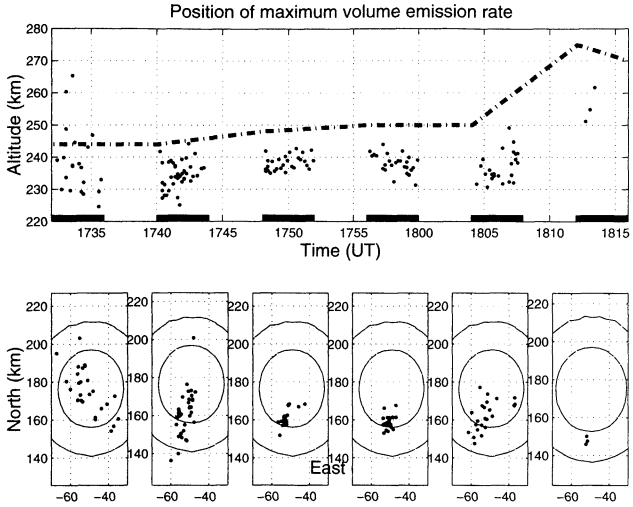

Figure 6. Upper panel shows the altitude of maximum enhanced airglow. Thick dashed line is the altitude of the enhanced ion line. Lower panels shows the horizontal location relative to Kiruna of the enhanced airglow region for the corresponding pulse. The dashed contours are the projections of the -1 and -3 dB free space antenna pattern projected to the reflection height.

tematically some 5 15 km below the enhanced ion line altitude. Further it can be noted that the periods showing the largest spread in altitude, starting at 17:32 UT and 18:04 UT, appear to occur in close connection with a rise in altitude of the enhanced ion line altitude. For the 17:32 UT pulse the enhanced ion line rose from 234 km at 17:28 UT to 244 km at 17:32 and for the 18:04 UT pulse the enhanced ion line rose from 250 km at 17:04 UT to 274 km at 18:12 UT.

4.5. Temporal intensity variations

The triangulation results show that the maximum enhancements occur 10 ± 5 km below the enhanced ion line for the period from 17:32 to 18:16 UT. Assuming that this result is valid for the entire experiment and that the altitude-averaged effective lifetime is very close to the effective lifetime at the altitude of maximum airglow emission it is possible to get an estimate of the altitude variation of the $O(^1D)$ effective lifetime.

To do this we apply equation (26) to the average over the entire region in the image where there are airglow enhancements. To remove the natural airglow variation we take the intensities in the points just before each HF-pump pulse on and use cubic spline interpolation for the background intensities at times in between. In Abisko there was cloud cover that thinned just before 17:00 UT but remained and varied slightly during the night. That made this straightforward approach to background reduction difficult to use for the period around 17:00 UT. For that period a cubic spline was fitted to the average intensities at times 16:59:35, 17:03:05, 17:03:45, 17:07:55, 17:11:55, 17:15:15 and 17:15:35 UT, giving the solid line in the top panel of Figure 7. With this background a reasonable estimate of the enhanced airglow intensity is obtained for the pulses between 17:00 and 17:14 UT. For the time just after the pump-off where the source of $O(^1D)$ excitation $\tilde{Q}(t) = 0$ it is possible to rearrange equation (26) [*Bernhardt et al.*, 2000] to

$$\tau_a = \frac{1}{\bar{D}(t)} \frac{\partial \bar{D}(t)}{\partial t} \tag{27}$$

where $\bar{D}(t)$ is the average enhanced imaged airglow. Applying this procedure to the enhanced image intensity we obtain estimates of the altitude-averaged $O(^1D)$ effective lifetime τ_a for each HF-pump pulse as is presented in Table 1.

When comparing the $O(^1D)$ effective lifetime it is found that the experimental estimates have a slightly slower increase with altitude than calculated with the quenching rates from section 3.2 and the MSIS-90 model atmosphere, as can be seen in Figure 8.

If we now apply the estimated $O(^1D)$ lifetimes to the initial portions of the respective HF-pulses we get a first order estimate of the time variation of the total excitation rate of $O(^1D)$. When doing this for the pulses during the period 17:32 to 18:30 UT a comparatively simple response emerges, as seen in Figure 9. The characteristics during the initial portion of the pulse is well modelled by $Q = Q_0 \cdot (1 - exp(-t/25))$. This confirms the finding in section 4.2 that the total excitation $Q(t)$ has a rise time of about 25 30 s.

Applying this method in order to estimate the time variation of $O(^1D)$ excitation for the pulses between 17:08 and 17:14 UT the response approximates boxcar functions, as can be seen in Figure 7. The rise times of 25–30 s obtained for the later pulses are absent and the

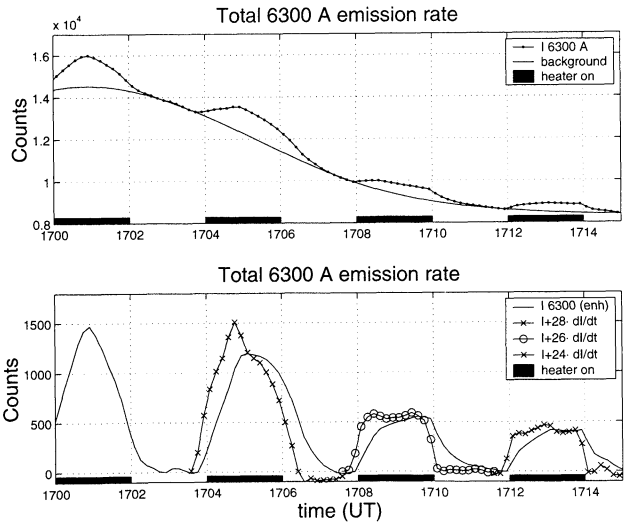

Figure 7. Upper panel: The total intensity of the airglow region and the estimated background. Lower panel shows the time variation of the artificially enhanced airglow and the estimated time variation of $O(^1D)$ excitation.

Table 1. Estimates of effective lifetime

HF-pulse UT	τ_a (s)	Altitude (km)	Stations
16:45 - 17:00	24 ± 3	220[b]	K
17:08	27 ± 3	215[b]	A
17:12	23 ± 6	225[b]	A
17:32	36 ± 3	235[a]	S, K
17:40	32 ± 3	234[a]	N, S, A
17:48	32 ± 3	238[a]	N, S, A
18:04	38 ± 10	236[a]	N, S
18:12	38 ± 4	253[a]	S
18:20	35 ± 4	234[b]	S

[a]Altitude from triangulation.
[b]Altitude from enhanced ion line -10 km.
A = Abisko, K = Kiruna, N = Nikkaluokta, S = Silkimuotka

excitation appears to reach steady state promptly, i.e. within 5 10 s. For the pulses between 17:00 and 17:06 UT the estimated time variation of excitation shows a smoother variation.

The small bump that appears shortly after the pump-off can be explained by the altitude variation in τ and the increase in $O(^1D)$ excitation by dissociative recombination, as described by equation (28).

5. Theoretical airglow modelling

There exist two main theoretical models for HF-pump enhanced airglow. One model suggests that the airglow is caused by $O(^1D)$ excitation of the high energy tail of a Maxwellian electron distribution [*Mantas*, 1994; *Mantas and Carlson*, 1996] and the other main model suggests that the $O(^1D)$ is caused by accelerated electrons [*Perkins and Kaw*, 1971; *Weinstock and Bezzerides*, 1974; *Weinstock*, 1975; *Gurevich et al.*, 1985]. In this section we will compare the existing theoretical models of enhanced airglow with the experimental data presented here.

The main ionospheric sources of $O(^1D)$ that are affected by the HF-pumping are dissociative recombination

$$O_2^+ + e_{th} \rightarrow O(^3P, ^1D, ^1S) \tag{28}$$

with a reaction rate [*Solomon et al.*, 1988]

$$\beta = 1.9 \cdot 10^{-7} \cdot (T_e/300)^{-0.5} \tag{29}$$

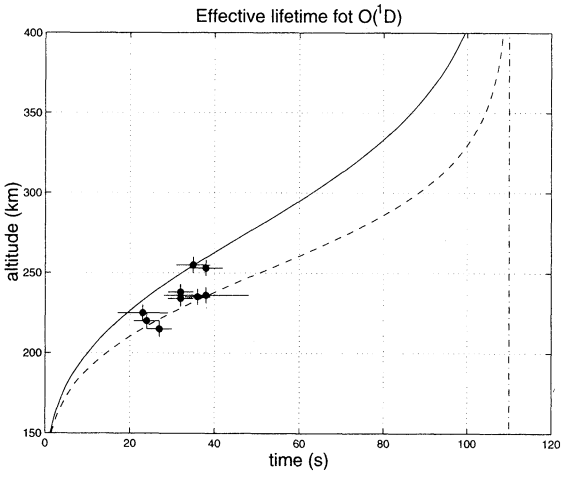

Figure 8. Altitude variation of $\tau_{O(^1D)}$. Dot-dashed line is the radiative lifetime of the $O(^1D)$. Dashed curve is the lifetime with quenching by O_2, N_2 and ambient electrons taken into account. Solid curve also includes quenching by atomic oxygen. The markers indicate estimates of $O(^1D)$ lifetimes obtained from the analysis in section 4, at the altitude determined by triangulation or altitudes 10 km below HF-pump wave enhanced ion line altitude.

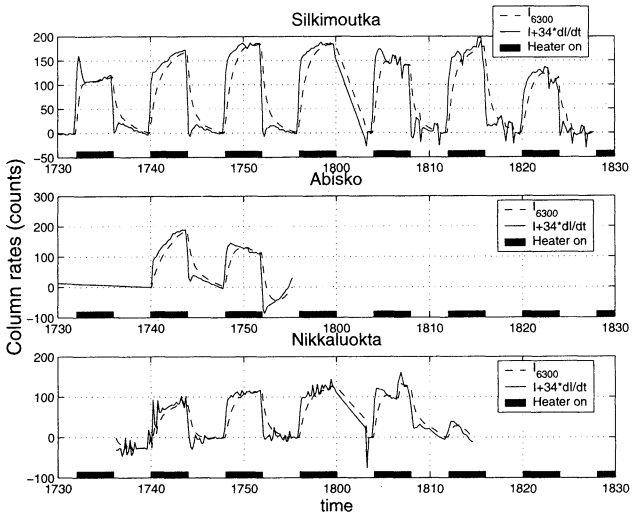

Figure 9. The total enhanced airglow (dashed) and the first order estimate of the time variation of the $O(^1D)$ excitation (solid). The upper panel shows the estimate from Silkimuotka data. The middle panel shows the estimates from Abisko data and the bottom panel shows estimates from Nikkaluokta data.

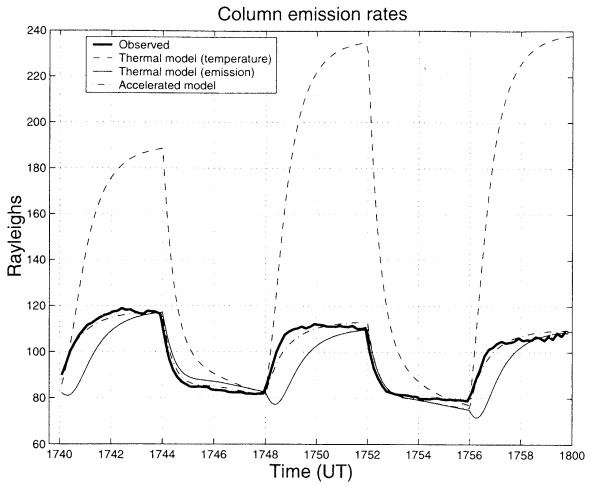

Figure 10. Measured (thick solid) and modeled column emission. The dashed curve is airglow emission calculated from the "hot temperature" profiles, the thin solid curve the airglow emission calculated from the "warm temperature" profiles, and the dot-dashed curve the airglow emission calculated with an electron distribution that corresponds to the "hot temperature" profile up to 2 eV and a constant isotropic electron source from 2–10 eV.

with a $O(^1D)$ yield of 1.2 atoms per reaction [*Abreu et al.*, 1986], and direct electron impact

$$O(^3P) + e(E > 1.96eV) \rightarrow O(^1D) + e \qquad (30)$$

with a reaction rate [*Mantas*, 1994]

$$\alpha(T_e) = 0.502 \cdot \sqrt{T_e} \frac{(9329 + T_e)}{(51813 + T_e)^3} \exp(-\frac{22756}{T_e}) \qquad (31)$$

for excitation from a thermal electron distribution. The increase in electron temperature caused by the HF-pump wave will decrease the reaction rate of dissociative recombination, equation (28), according to equation equation (29), and provided that the electron distribution remains Maxwellian over the energy range 2 10 eV, increase the rate coefficient of equation (30). The HF-pump wave induced variation in 6300 Å airglow will then be determined by the relative importance of the two reactions. To model the 6300 Å airglow response to the HF-pump we need accurate calculations of the ionosphere-thermosphere composition and temperature. For a detailed modelling of the 6300 Å airglow we use a time-dependent one-dimensional ionospheric model. In this model we solve the coupled time-dependent continuity equations for the minor neutral species, $O(^1D), O(^1S), N(^4S), N(^2P), N(^2D), N(^2P), NO$ and the ions O_2^+, NO^+, N_2^+, O^+ the equation of motion for ions and electrons as well as the electron and ion energy equations. Input parameters of the model are the neutral composition and temperature, MSIS-90 atmospheric model [*Hedin*, 1991], the ultraviolet solar flux and precipitating particle flux. A more exhaustive description of the source and loss processes of the other minor species included in this model as well as the numerical methods used in solving the equations is outside the scope of this report.

To obtain the initial conditions most important the ion composition of the lower F-region ionosphere the equations are solved from 12:00 UT with input of the MSIS neutral atmosphere for the prevailing geophysical conditions.

To test the thermal hypothesis, where the electron distribution is assumed to remain Maxwellian during the interaction with the HF-pump wave [*Biondi et al.*, 1970; *Mantas*, 1994; *Mantas and Carlson*, 1996; *Gurevich and Milikh*, 1997] and the excitation of $O(^1D)$ is caused by the thermal tail above 1.96 eV, we search for a heat source that reproduces the EISCAT UHF electron temperature measurements between 17:40 and 18:04 UT, both concerning the time variation and altitude distribution. The best fit with the EISCAT UHF data is obtained with a 5 km wide heat source of $6 \cdot 10^4$ $eV/m^3/s$ at an altitude of 220 km for which both the altitude and the temporal variation of the electron temperature agree well with what is observed, as shown in the Plate 8 where the measured electron temperature for the period 17:40 to 18:04 UT is plotted in the upper panel and the modelled electron temperature, henceforth denoted as the "hot temperature", from this source, is plotted in the middle panel. The $O(^1D)$ emission caused by excitation of the high energy tail of the hot temperature electron distribution corresponds to an increase of about 200 % above the background compared to the observed increase that is only between

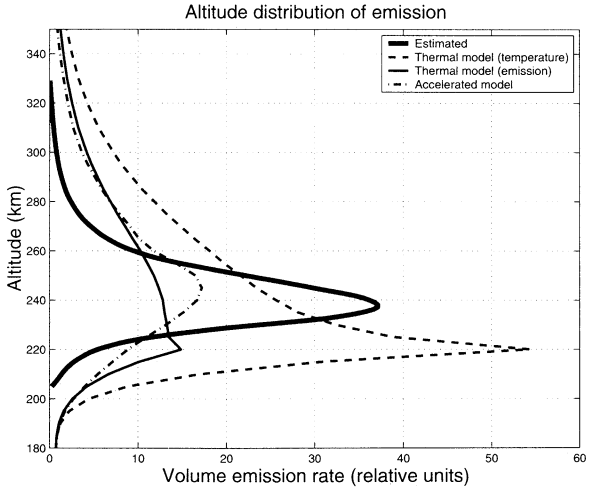

Figure 11. Comparison between estimated and modelled altitude distribution of the 6300 Å emission. The thick solid curve is the estimated altitude distribution of 6300 Å emission. The dashed curve is the airglow modelled with excitation from the high energy tail of a Maxwellian electron distribution with the 'hot electron temperature'. The thin solid curve is the airglow distribution as above but with the 'warm electron temperature'. The dot-dashed curve is the airglow distribution from an isotropic source at the altitude of the enhanced ion line.

50 and 70 %. Furthermore neither the time variation, where the modelled intensity growth does not level off as markedly as the observed (as is seen in Figure 10) nor the altitude distribution plotted in Figure 11, agrees very well with what is observed. In particular the altitude of maximum emission is at too low an altitude by 18 km.

The opposite approach, to search for a heat source that gives a good fit with the optical data, results in an estimated heat source of $4{\cdot}10^{1}\ eV/m3/s$. This also leads to incompatibilities. There is an initial lag time in the $O(^1D)$ 6300 Å airglow due to an initial decrease in the source from dissociative recombination, and the calculated electron temperature (henceforth denoted "warm temperature") is systematically lower than the electron temperatures observed by the EISCAT UHF radar (as can be seen in the bottom panel of Plate 8) for all times and all altitudes, especially the peak temperature that is now only approximately 3070 K compared to the measured 3500 K.

The other main hypothesis is that the enhanced excitation of $O(^1D)$ is due to a non-thermal electron distribution in the energy range 2–10 eV. It has been suggested that the source of this distribution is acceleration of electrons by Langmuir turbulence [*Meltz and Perkins*, 1974; *Gordon and Carlson*, 1974; *Gurevich et al.*, 1985; *Bernhardt et al.*, 1989b]. To model the $O(^1D)$ 6300 Å airglow response to this source, we assume an electron source at the same altitude as the altitude of the HF-pump wave enhanced ion line altitude with isotropic flux and a uniform energy distribution in the range 2 – 10 eV. The excitation rate of $O(^1D)$ from this source is calculated with a Monte-Carlo model of the electron transport in the Earth's atmosphere [*Ivanov and Sergienko*, 1992]. The $O(^1D)$ excitation from equation (28) is taken into account, while the contribution from direct impact excitation of the thermal electrons is absent in this case. An electron source with an energy flux of $1.8 \cdot 10^{9} eV cm^{-2} s^{-1}$ gives a 6300 Å emission that has the best agreement with the observed emissions.

The direct $O(^1D)$ excitation rate α (equation (31)) can be written as

$$\alpha \propto \int_{1.96}^{\infty} E f(E) \sigma(E) dE \qquad (32)$$

where E is the electron energy in eV, $f(E)$ is the electron distribution function, and $\sigma(E)$ is the integral excitation cross section for direct electron excitation of $O(^1D)$. Since the modelled enhancement of the column emission from the hot temperature is approximately a factor of three larger than observed we can conclude that

$$\int_{1.96}^{\infty} E f(E) \sigma(E) dE \approx 0.3 \int_{1.96}^{\infty} E f_{th}(T_e, E) \sigma(E) dE \qquad (33)$$

where $f_{th}(E, T_e)$ is a Maxwellian electron distribution with electron temperature T_e. With only measurements of 6300 Å airglow it is not possible to determine the shape of the high energy tail of the electron distribution. A consequence of the above relation is, however, that the main characteristic of the electron distribution from 2 10 eV is a depletion, as shown in Figure 12, i.e. the electron distribution function is found to be sub-thermal during ionospheric HF-pumping.

One likely reason for this is the energy loss of 2–3 eV electrons to the vibrational levels of N_2. It has long been known that this electron excitation of the vibrational states of N_2 is strong and and several authors [*Rees*, 1989; *Bernhardt et al.*, 1989b] have reported it to peak between $1 \cdot 10^{-16}$ and $3 \cdot 10^{-16} cm^2$ for 2–3 eV electrons. The effect of electron excitation of the N_2 vibrational states has been calculated to produce significant dips in the electron spectra both during precipitation of high energy electrons [*Rees*, 1989] and for photoelectrons [*Nilsson et al.*, 1996], even at 250 km altitude; the same process should cause a decrease in the electron energy distribution relative to the purely thermal case also during HF-pump experiments.

6. Summary and discussion

In this paper we present the first estimates of the three-dimensional distribution of HF-pump wave enhanced $O(^1D)$ 6300 Å airglow, with data from the experiment on 16th February 1999. The altitude of maximum emission is found to vary from 230 240 km between 17:32 and 18:08 UT to 250 260 km between 18:12 and 18:16 UT. The enhanced airglow is approximately 10 km below the altitude of the HF-pump wave enhanced ion line altitude. For the two HF-pump pulses

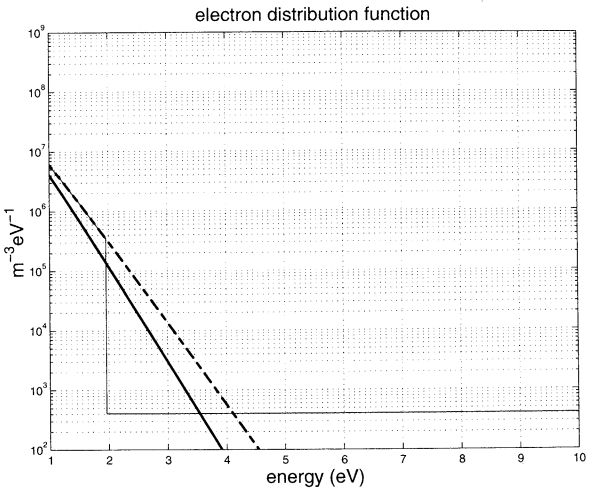

Figure 12. Thick solid curve denotes the Maxwellian energy distribution for $T_e = 3000K$, the dashed curve denotes Maxwellian energy distribution for $T_e = 3500K$, and the thin solid curve denotes a Maxwellian energy distribution for energies up to 1.96 eV and Constant above. The Constant density is adjusted to give agreement with the observed airglowq.

between 17:40 and 17:52 UT an estimate of the three-dimensional distribution of the 6300 Å emission was achieved by a tomography-like inversion. The shape of the emission region varied between slightly oblate to clearly prolate aligned along the magnetic field. The e-folding width of the emission region varies from 17 to 22 km in the horizontal plane and from 12 to 27 km in the vertical direction.

For the time period between 17:40:00 to 17:44:00 UT we show that there exist two regions of excitation simultaneously growing and merging. It appears as if the initially more intensive region starts to grow close to the projection of the maximum of the HF-pump beam while the initially weaker region starts to grow close to the -3 dB upwind edge of the HF-pump wave field, approximately 30 km to the south. The drift of the "center of excitation" of the initially weaker region is estimated to be 30 ± 5 km northward during the 4 minute HF-pump pulse.

A recurring pattern seen after HF-pump on is that the initial excitation is speckled but after some 25 seconds the shape of the excitation is simpler. It also appears as if there is a tendency for the upwind patches to grow and drift into the central region while the downwind regions fade and drift out of the beam.

From a comparison of the observed and modeled time variations of the enhanced airglow it is seen that a thermal electron distribution with electron temperature from the EISCAT UHF measurements produce enhancements in 6300 Å airglow that are a factor of 2.5 4 too large. The time variation is more accurately reproduced by an electron distribution that is thermal below 1.9 eV and a constant isotropic source of electrons with energies between 2 and 10 eV. For the high electron temperatures, 3000 3500 K, this implies that the artificially enhanced 6300 Å airglow is excited by a sub-thermal electron distribution, for which the high energy tail rapidly saturates.

Thus from our observations during the HF-pump experiment on 16th February 1999 we can make a plausible claim that the enhanced airglow is not excited by the high energy tail from a purely Maxwellian electron distribution. The main experimental findings supporting this conclusion are:

1. The large overestimate by a factor of 2.5 to 4 of the predicted airglow from thermal models and the observed enhanced airglow.

2. The complete lack of lag time or initial decrease of the 6300 Å $O(^1D)$ airglow that is expected during initial electron warming up due to a decrease of dissociative recombination.

3. The altitudes of maximum electron temperature and the altitude of maximum emission differ by as much as 20 km.

4. The altitude distribution of excitation and emission is in slightly better agreement with the excitation of $O(^1D)$ by accelerated electrons.

These observations raise the following questions to be addressed in future experiments:

- What physical processes control the complex drift pattern.
- What physical processes control the transition from the initial complex excitation structure.
- During what physical conditions can more than one region of strong $O(^1D)$ excitation coexist.

Acknowledgments. The author would like to thank two unknown referees for their valuable comments and suggestions.

ALIS is funded by FRN (Forskningsrdsnmnden), NFR (Nationella forskningsrdet), Swedish National Space board, (Rymdstyrelsen, fjrranalyskommitén) and IRF (Swedish Institute of Space Physics). EISCAT is an International Association supported by Finland (SA), France (CNRS), the Federal Republic of Germany (MPG), Japan (NIPR), Norway (NFR), Sweden (NFR) and the United Kingdom (PPARC).

References

Abreu, V. J., J. H. Yee, S. C. Solomon, and A. Dalgarno, The quenching rate of $O(^1D)$ by $O(^3P)$, *Planet. Space Sci.*, *11*, 1143, 1986.

Adeishvili, T. G., A. V. Gurevich, S. B. Lyakhov, G. G. Managadze, G. M. Milikh, and I. S. Shluyger, Ionospheric emisson caused by an intense radio wave, *Sov. J. Plasma Phys.*, *4*, 721, 1978.

Aruliah, A., A. Farmer, D. Rees, and U. Brändström, The seasonal behaviour of high-latitude thermospheric winds and ion velocities observed over one solar cycle, *J. Geophys. Res.*, *101*, 15701–15711, 1996.

Aso, T., M. Ejiri, A. Urashima, H. Miyaoka, Å. Steen, U. Brändström, and B. Gustavsson, First results of auroral tomography from ALIS-Japan multi-station observations in March 1995, *Earth Planets and Space*, *50(1)*, 63–80, 1998.

Belur, S. V., An optimized step size random search method, *Computer Methods in Applied Mechanics and Engineering*, *19*, 99–106, 1979.

Bernhardt, P. A., Three-dimensional, time-dependent modeling of neutral gas diffusion in a nonuniform, chemically reactive atmosphere, *J. Geophys. Res.*, *84*, 793–802, 1979.

Bernhardt, P. A., L. M. Duncan, and C. A. Tepley, Heater induced cavities as optical tracers of plasma drift, *J. Geophys. Res.*, *94*, 7003–7010, 1989a.

Bernhardt, P. A., C. A. Tepley, and L. M. Duncan, Airglow enhancements associated with plasma cavities formed during ionospheric heating experiments, *J. Geophys. Res.*, *94*, 9071–9092, 1989b.

Bernhardt, P. A., M. Wong, J. D. Huba, B. G. Fejer, L. S. Wagner, J. A. Goldstein, C. A. Selcher, V. L. Frolov, and E. N. Sergeev, Optical remote sensing of the thermosphere with HF pumped artificial airglow, *J. Geophys. Res.*, *105*, 10657–10671, 2000.

Biondi, A. A., D. P. Sipler, and R. D. Hake, Optical (λ – 6300) detection of radio frequency heating of electrons in the F region, *J. Geophys. Res.*, *75*, 6421–6424, 1970.

Brändström, B. U. E., T. B. Leyser, Å. Steen, M. T. Rietveld, B. Gustavsson, T. Aso, and M. Ejiri, Unambigu-

ous evidence of HF pump-enhanced airglow at auroral latitudes, *Geophys. Res. Lett.*, *26*, 3561 3564, 1999.

Carlson, H. C., V. B. Wickwar, and G. P. Mantas, Observations of suprathermal electrons accelerated by HF-excited instabilities, *J. Atmos. Terr. Phys.*, *44*, 1089 1100, 1982.

Duncan, L. M., and R. A. Behnke, Observations of self-focusing electromagnetic waves in the ionosphere, *Phys. Rev. Lett.*, *41*, 998 1001, 1978.

Farley, D. T., C. LaHoz, and B. G. Fejer, Studies of the self-focusing instability at arecibo, *J. Geophys. Res.*, *88*, 2093 2102, 1983.

Fischer, C. F., and H. P. Saha, Multiconfiguration Hartree-Fock results with Briet-Pauli corrections for forbidden transitions in the $2p^4$ configuration, *Phys. Rev. A*, *28*, 3169, 1983.

Ghosh Roy, D. N., *Methods of Inverse Problems in Physics*, CRC Press, Boca Raton, Fla., 1991.

Gordon, W. E., and H. C. Carlson, Arecibo heating experiments, *Radio Sci.*, *9*, 1041–1047, 1974.

Gurevich, A. V., and G. M. Milikh, Artificial airglow due to modifications of the ionosphere by powerful radio waves, *J. Geophys. Res.*, *102*, 389–394, 1997.

Gurevich, A. V., Y. S. Dimant, G. M. Milikh, and V. V. Va'skov, Multiple acceleration of electrons in the regions high power radio-wave reflection in the ionosphere, *J. Atmos. Terr. Phys.*, *47*, 1057 1070, 1985.

Gustavsson, B., Tomographic inversion for ALIS noise and resolution, *J. Geophys. Res.*, *103*, 26,621–26,632, 1998.

Haslett, J. C., and L. R. Megill, A model of the enhanced airglow excited by rf-radiation, *Radio Sci.*, *9*, 1005–1019, 1974.

Hedin, A., Extension of the MSIS thermospheric model into the middle and lower atmosphere, *J. Geophys. Res.*, *96*, 1159–1172, 1991.

Honary, F., A. J. Stocker, T. R. Robinson, T. B. Jones, N. M. Wade, P. Stubbe, and H. Kopka, EISCAT observations of electron temperature oscillations due to the action of high power HF radio waves, *J. Atmos. Terr. Phys.*, *55*, 1433 1448, 1993.

Ivanov, V. E., and T. I. Sergienko, *Interaction of the auroral electrons with the atmospheric gases. (The Monte-Carlo modeling)*, Nauka, St. Petersburg, 1992.

Leyser, T. B., B. Gustavsson, B. U. E. Brändström, Å. Steen, F. Honary, M. T. Rietveld, T. Aso, and M. Ejiri, Simultaneous measurements of high-frequency pump-enhanced airglow and ionospheric temperatures at auroral latitudes, *Adv. Polar Upper Atm. Res.*, pp. 1–11, 2000.

Link, R., and L. L. Cogger, A reexamination of the OI 6300-Å nightglow, *J. Geophys. Res.*, *93*, 9883–9892, 1998.

Mantas, G. P., Large 6300-Å airglow intensity enhancements observed in ionosphere heating experiments are excited by thermal electrons, *J. Geophys. Res.*, *99*, 8993, 1994.

Mantas, G. P., and H. C. Carlson, Reinterpretation of the 6300-Å airglow enhancements observed in ionosphere heating experiments based on analysis of Platteville, Colorado, data, *J. Geophys. Res.*, *101*, 195 209, 1996.

Meltz, G., and F. W. Perkins, Ionospheric modification theory: Past, present and future, *Radio Sci.*, *9*, 885–888, 1974.

Nilsson, H., S. Kirkwood, J. Lilensten, and M. Galand, Enhanced incoherent scatter plasma lines, *Ann. Geophys.*, *14*, 1462–1472, 1996.

Perkins, F. W., and P. K. Kaw, On the role of plasma instabilities in ionospheric heating by radio waves, *J. Geophys. Res.*, *76*, 282–284, 1971.

Rees, M. H., *Physics and Chemistry of the Upper Atmosphere*, Cambridge Univ. Press, New York, 1989.

Rietveld, M. T., H. Kohl, H. Kopka, and P. Stubbe, Introduction to ionospheric heating at Tromsø I. experimental overview, *J. Atmos. Terr. Phys.*, *55*, 577–599, 1993.

Semeter, J., Ground based tomography of atmospheric optical emissions, Ph.D. thesis, Boston University, Boston, MA, 1997.

Sergienko, T., B. Gustavsson, Å. Steen, U. Brändström, M. Rietveld, and T. Leyser, Analysis of excitation of the 630.0 nm airglow during heating experiment in Tromsø on February 1999, *Physics and Chemistry of the Earth*, 2000.

Sipler, D. P., and M. A. Biondi, Measurements of $O(^1D)$ quenching rates in the F region, *J. Geophys. Res.*, *77*, 6202 6212, 1972.

Solomon, S. C., P. B. Hays, and V. J. Abreu, The auroral 6300 Å emission: Observation and modeling, *J. Geophys. Res.*, *93*, 9867 9882, 1988.

Steen, Å., and U. Brändström, A multi-station ground-based imaging system at high latitudes, *STEP Int. Newsl.*, *3*, 11 14, 1993.

Stubbe, P., Review of ionospheric modification experiments at tromsø, *J. Atmos. Terr. Phys.*, *58*, 349 368, 1996.

Stubbe, P., et al., Ionospheric modification experiments in northern Scandinavia, *J. Atmos. Terr. Phys.*, *44*, 1025–1041, 1982.

Weinstock, J., Theory of enhanced airglow during ionospheric modifications, *J. Geophys. Res.*, *80*, 4331, 1975.

Weinstock, J., and B. Bezzerides, Theory of electron acceleration during parametric instabilities, *Phys. Rev. Lett.*, *32*, 754–758, 1974.

B. Gustavsson (e-mail: bjorn.gustavsson@irf.se), T. Sergienko (e-mail: tima.sergienko@irf.se), Å. Steen (e-mail: ake.steen@irf.se) and U. Brändström (e-mail: urban.brandstrom@irf.se), Swedish Institute of Space Physics, Box 812, SE-981 28 Kiruna, Sweden.

M. Rietveld (e-mail: Mike.Rietveld@eiscat.uit.no), Max-Planck Institut für Aeronomie, D-37191 Katlenburg Lindau, Germany, also at EISCAT, N-9027, Ramfjordbotn, Norway.

T. Leyser (e-mail: thomas.leyser@irfu.se), Swedish Institute of Space Physics, Uppsala division, SE-755 91 Uppsala, Sweden.

F. Honary, Department of Communication systems, Lancaster University, UK.

A. L. Aruliah (e-mail: a.aruliah@ucl.ac.uk), Atmospheric Physics Lab., University College London, 67-73, Riding House St., London W1P 7PP, England.

T. Aso (e-mail: aso@nipr.ac.jp) and M. Ejiri (e-mail: ejiri@nipr.ac.jp), National Institute of Polar Research, Arctic Environment Research Center, Tokyo 173-8515 Japan.

S. Marple, Department of Communication systems, Lancaster University, UK.

(Received August 2, 2000; revised November 2, 2000;
accepted November 26, 2000.)